THE PHOTOGRAMMETRIC RECORD

The Photogrammetric Record 35(170): 123–142 (June 2020)
DOI: 10.1111/phor.12315

GEOMETRIC MODELLING AND CALIBRATION OF A SPHERICAL CAMERA IMAGING SYSTEM

Derek D. Lichti* (ddlichti@ucalgary.ca)
David Jarron (dmjarron@ucalgary.ca)
Wynand Tredoux (wynand.tredoux@ucalgary.ca)
Mozhdeh Shahbazi (Mozhdeh.shahbazi@ucalgary.ca)
University of Calgary, Calgary, Canada

Robert Radovanovic (rradovanovic@mcelhanney.net)
McElhanney Ltd., Calgary, Canada

**Corresponding author*

Abstract

The Ladybug5 is an integrated, multi-camera system that features a near-spherical field of view. It is commonly deployed on mobile mapping systems to collect imagery for 3D reality capture. This paper describes an approach for the geometric modelling and self-calibration of this system. The collinearity equations of the pinhole camera model are augmented with five radial lens distortion terms to correct the severe barrel distortion. Weighted relative orientation stability constraints are added to the self-calibrating bundle adjustment solution to enforce the angular and positional stability between the Ladybug5's six cameras. Centimetre-level 3D reconstruction accuracy can be achieved, with image-space precision and object-space accuracy improved by 92% and 93%, respectively, relative to a two-term lens distortion model. Sub-pixel interior orientation stability and millimetre-level relative orientation stability were also demonstrated over a 10-month period.

Keywords: camera calibration, Ladybug5, multi-camera system, relative orientation stability, wide-angle lenses

Introduction

State-of-the-art mobile mapping systems (MMSs) comprise multiple sensors for mapping complex terrestrial environments. In addition to navigation sensors (Global Navigation Satellite System (GNSS) receivers, inertial measurement units and so on) for trajectory determination, they generally include multiple imaging sensors such as laser scanners and digital cameras. Whether the MMS is vehicle-borne or backpack based, the Ladybug imaging systems from FLIR Integrated Imaging Solutions are a common choice to facilitate panoramic imaging in support of 3D reality capture. These systems, in particular the Ladybug3 and Ladybug5, comprise six cameras integrated in a rigid housing to provide a nearly spherical field of view. In their review of urban applications and methods, Wang et al. (2019) summarise eight MMS systems, of which five include Ladybug5 devices. Others report MMSs incorporating Ladybug cameras on robotic (Schneider and Förstner, 2013), backpack (Rau et al., 2016) and land vehicle (Cui et al., 2017) platforms.

Despite the seemingly widespread use of these camera systems, few detailed reports exist about their geometric calibration. Schneider and Förstner (2013) report on the self-calibration of a Ladybug3 system. In particular, they comment on deviations of the relative orientation between cameras from the manufacturer's values. Rau et al. (2016) describe the self-calibration of the Ladybug5. They mention the need for higher-order radial lens distortion terms and report large residual systematic errors. Bosch et al. (2015) describe a ray-tracing approach for underwater use of a Ladybug3 system. Jarron et al. (2019a) provide a brief, initial report on the self-calibration of the Ladybug5. Much more detailed treatment is given herein.

The purpose of this paper is to present a geometric modelling approach and calibration assessment of a multi-camera imaging system, specifically, the FLIR Ladybug5. The system in question is first described in detail in order to give proper context to the mathematical modelling. Next, the geometric models used for the system observation equations, constraints and lens distortions are described. Experiments to test the effectiveness of the modelling approach are then described. The results and analyses that follow comprise several quantitative assessments:

(1) the quality of the interior orientation parameters;
(2) the effectiveness of the radial lens distortion model;
(3) the quality of the relative orientation parameters; and
(4) the 3D measurement accuracy as a result of the modelling approach.

Camera System Description

The Ladybug5 Spherical Camera Imaging System from FLIR Integrated Imaging Solutions comprises six cameras integrated in a rigid housing (Fig. 1). Each camera is a Sony ICX655 (2/3″ charge-coupled device (CCD); 3·45 μm pixel size; 2048×2448 pixel count; global shutter) fitted with a 4·4 mm focal length lens. The system can output uncompressed imagery at 5 Hz or JPEG imagery at 10 Hz.

The horizontal cameras are mounted with a roll angle of 90° so that the long dimension of the sensor format is vertically oriented. As a result, the corresponding horizontal and vertical angular fields of view of each camera are approximately 77·5° and 87·6°, respectively. The angular overlap between any two adjacent horizontal cameras is approximately 5·5°. Their perspective centres nominally lie on a horizontal circle with an approximate radius of 60 mm. The sixth camera is oriented so that it looks vertically upwards; its perspective centre is nominally 75 mm above the plane containing those of the horizontal cameras. The overlap of the vertical camera with the horizontal cameras' fields of view varies due to the rectangular image format.

Methodology

Collinearity Equations

The imaging geometry of a multi-camera system comprising n cameras is described by two sets of parameters: the n sets of individual cameras' interior orientation parameters (IOPs); and the $(n-1)$ sets of relative orientation parameters (ROPs) between cameras. Observations in each individual camera are modelled by the collinearity condition that

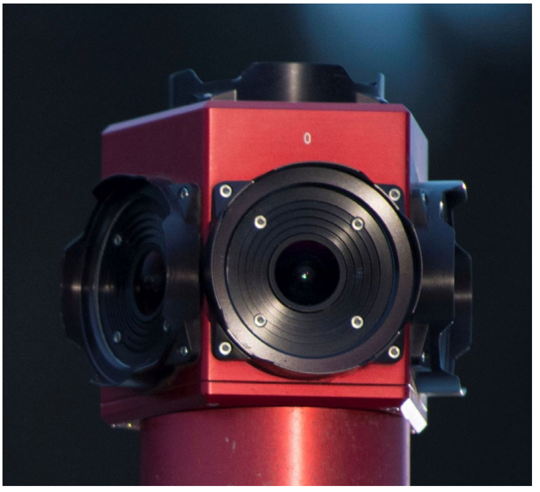

FIG. 1. The Ladybug5 system (image courtesy McElhanney Ltd).

expresses the hypothesised straight-line relationship between object point i (X, Y, Z), its image point (x, y) and the perspective centre of image j (X^c, Y^c, Z^c):

$$x_{ij} + \varepsilon_{x_{ij}} = x_{p_j} - c_j \frac{m_{11}(X_i - X_j^c) + m_{12}(Y_i - Y_j^c) + m_{13}(Z_i - Z_j^c)}{m_{31}(X_i - X_j^c) + m_{32}(Y_i - Y_j^c) + m_{33}(Z_i - Z_j^c)} + \Delta x_{ij} \tag{1}$$

$$y_{ij} + \varepsilon_{y_{ij}} = y_{p_j} - c_j \frac{m_{21}(X_i - X_j^c) + m_{22}(Y_i - Y_j^c) + m_{23}(Z_i - Z_j^c)}{m_{31}(X_i - X_j^c) + m_{32}(Y_i - Y_j^c) + m_{33}(Z_i - Z_j^c)} + \Delta y_{ij} \tag{2}$$

where (x_p, y_p) are the coordinates of the principal point, c is the principal distance, and m_{pq} are elements of the rotation matrix $\mathbf{M}$, which is parameterised in terms of the sequential rotation angles ω, ϕ and κ.

Lens Distortion Modelling

The collinearity equations are augmented with both random error terms (ε_x, ε_y) and correction terms (Δx, Δy) that model the systematic errors that cause departures from collinearity due to lens distortion. The standard, two-term (p_1, p_2) Brown–Conrady model is employed to model decentring distortion (Brown, 1966, 1971):

$$\Delta x = p_1(r^2 + 2\bar{x}^2) + 2p_2\overline{xy} \tag{3}$$

$$\Delta y = p_2(r^2 + 2\bar{y}^2) + 2p_1\overline{xy} \tag{4}$$

where r is radial distance with respect to the principal point and ($\bar{x}$,$\bar{y}$) are image coordinates reduced to the principal point.

The severe barrel distortion inherent to the wide-angle lenses of the Ladybug5 system requires five radial lens distortion terms (k_1, k_2, k_3, k_4, k_5):

$$\Delta x = \bar{x}(k_1 r^2 + k_2 r^4 + k_3 r^6 + k_4 r^8 + k_5 r^{10}) \quad (5)$$

$$\Delta y = \bar{y}(k_1 r^2 + k_2 r^4 + k_3 r^6 + k_4 r^8 + k_5 r^{10}). \quad (6)$$

Though the use of more than three radial lens distortion coefficients is not commonly encountered, some software packages support inclusion of higher-order terms. Both the FLIR Ladybug5 SDK and Agisoft PhotoScan/Metashape (Agisoft LLC, 2018) support inclusion of the k_4 term while Photometrix CameraCalibrator supports the addition of both k_4 and k_5 (Photometrix, 2016).

Colour cameras can also possess chromatic aberrations due to light dispersion in the lens. It can have both longitudinal and transverse components. The former amounts to wavelength-dependent plane of best focus (principal distance) and the latter is wavelength-dependent radial lens distortion. An experiment to quantify the presence of chromatic aberration in the Ladybug5 system is reported in Lichti et al. (2019c). No significant longitudinal chromatic effects were found and the lateral effect was only at the 1 to 2 pixel level. Accordingly, these effects are omitted from the camera modelling herein.

Model Identification

A sequential model construction process is followed to identify significant terms in the radial lens distortion model. An initial self-calibrating bundle adjustment comprising a minimal set of IOPs is first performed. Generally, this might only include the principal distance and the principal point and, perhaps, k_1. For the Ladybug5, it also included k_2 due to the very high barrel distortion. Statistical, graphical and information-theoretical analyses are then performed. The radial component of the image point residuals is plotted as a function of radial distance. If a systematic trend can be observed in the scatter plot, the distortion model is augmented by one term and the self-calibration adjustment is run again with the new model. The root mean square of the residuals, RMS_{xy} (Remondino et al., 2017), is computed and analysed.

If the added term is significant, then RMS_{xy} should be reduced by a significant amount. Judging the significance of the reduction to RMS_{xy} can be subjective and the parameter significance test ignores inherent parameter correlations. Therefore, some additional measures are computed. First, the statistical significance of each lens distortion parameter is examined using the univariate testing procedure described by Shortis et al. (2000). Second, the Akaike Information Criterion (AIC; Akaike, 1974) is used to ascertain whether the new model is superior to the previous. If a systematic trend is still visible in the new set of residuals, then the model complexity is increased and the process repeated until all trends have been modelled. Accuracy assessment using independently surveyed check points can also be performed to measure the significance of the model improvement in object space.

Relative Orientation Stability

Several approaches exist for modelling the relative orientation of multi-camera systems. An exhaustive review of all such methods is beyond the scope of this paper, so interested readers are referred to Detchev et al. (2018). Broadly speaking, they can be summarised as belonging to one of two approaches:

(1) explicitly modelled relative orientation; and
(2) added constraints that enforce stability of the ROPs.

Each approach makes the assumption that the relative position and orientation of the cameras in their housing are mechanically stable.

In the first approach, one camera of the system is designated as the master camera and the remaining sensors are designated as slave cameras. The exterior orientation parameters (EOPs) of the master camera and the ROPs of the $(n-1)$ cameras are estimated simultaneously. There is no need to derive the ROPs after the self-calibrating bundle adjustment since they explicitly appear in the model. Examples of this approach to modelling multi-camera systems can be found for mobile mapping (Habib et al., 2011) and laboratory-based, structural deformation measurement (Detchev et al., 2018).

The second modelling approach includes n sets of EOPs. The ROPs are not explicitly modelled. Instead, constraints are added to the multistation bundle adjustment to express the assumed relative stability of the cameras. The actual ROPs are derived from the EOPs post-adjustment. Three position and three angular constraints can be written between each camera pair. A total of $6(n-1)$ independent constraint equations can be added to the self-calibration adjustment. This is the approach adopted for this work. It has been applied to airborne multi-camera sensors (Tommaselli et al., 2013), multi-camera fisheye lens systems (Campos et al., 2018), a general multi-projective system (Khoramshahi and Honkavaara, 2018), an underwater stereo camera system (Shortis, 2015) and a dual fluoroscopic imaging system (Lichti et al., 2015).

The base vector (b_X, b_Y, b_Z) between cameras i and j can be defined as:

$$\begin{pmatrix} b_X \\ b_Y \\ b_Z \end{pmatrix}_{ij} = \mathbf{M}_i \begin{pmatrix} X_j^c - X_i^c \\ Y_j^c - Y_i^c \\ Z_j^c - Z_i^c \end{pmatrix}. \tag{7}$$

Note that the choice of image space in which the constraint is parameterised is arbitrary; camera i has been used here. The stability of the base vector components between cameras i and j is enforced by constraining the difference in their base vector components at two camera locations (1 and 2) to be zero:

$$\mathbf{M}_{i_1} \begin{pmatrix} X_j^c - X_i^c \\ Y_j^c - Y_i^c \\ Z_j^c - Z_i^c \end{pmatrix}_1 - \mathbf{M}_{i_2} \begin{pmatrix} X_j^c - X_i^c \\ Y_j^c - Y_i^c \\ Z_j^c - Z_i^c \end{pmatrix}_2 = \begin{pmatrix} 0 \\ 0 \\ 0 \end{pmatrix} + \begin{pmatrix} \varepsilon_{\Delta b_X} \\ \varepsilon_{\Delta b_Y} \\ \varepsilon_{\Delta b_Z} \end{pmatrix}_{12}. \tag{8}$$

Others (Lerma et al., 2010; Tommaselli et al., 2013) report the option to constrain the base vector length rather than its three components.

The development of the angular ROP stability constraints requires the intermediate computation of the relative rotation matrix, which can be parameterised in terms of relative angles $\Delta\omega$, $\Delta\phi$ and $\Delta\kappa$:

$$\Delta\mathbf{M}_{ij} = \mathbf{M}_j\mathbf{M}_i^{\mathrm{T}} = \mathbf{R}_3(\Delta\kappa_{ij})\mathbf{R}_2(\Delta\phi_{ij})\mathbf{R}_1(\Delta\omega_{ij}). \tag{9}$$

The constraints can be formulated in terms of the ROP angles themselves (Lichti et al., 2015) or as functions of the relative rotation matrix elements (King, 1995; Tommaselli et al., 2013). Here, the relative angles are constrained. Though the choice is perhaps somewhat subjective, the primary motivation is that the weighting (see below) for this approach is more intuitive because the constraint standard deviations can be expressed in angular units such as arc seconds rather than unitless direction cosines. The relative angles can be derived from $\Delta\mathbf{M}_{ij}$ according to the standard equations:

$$\Delta\omega_{ij} = \arctan\left(\frac{-\Delta m_{32}}{\Delta m_{33}}\right) \tag{10}$$

$$\Delta\phi_{ij} = \arcsin(\Delta m_{31}) \tag{11}$$

$$\Delta\kappa_{ij} = \arctan\left(\frac{-\Delta m_{21}}{\Delta m_{11}}\right). \tag{12}$$

It should be noted that an alternative angle parameterisation is required to avoid the gimbal lock problem if the secondary relative rotation angle is 90°.

The angular stability constraints enforce the differences between the relative angles between cameras i and j captured at locations 1 and 2 to be zero:

$$\begin{pmatrix} \arctan\left(\frac{-\Delta m_{32}}{\Delta m_{33}}\right) \\ \arcsin(\Delta m_{31}) \\ \arctan\left(\frac{-\Delta m_{21}}{\Delta m_{11}}\right) \end{pmatrix}_1 - \begin{pmatrix} \arctan\left(\frac{-\Delta m_{32}}{\Delta m_{33}}\right) \\ \arcsin(\Delta m_{31}) \\ \arctan\left(\frac{-\Delta m_{21}}{\Delta m_{11}}\right) \end{pmatrix}_2 = \begin{pmatrix} 0 \\ 0 \\ 0 \end{pmatrix} + \begin{pmatrix} \varepsilon_{\Delta\Delta\omega} \\ \varepsilon_{\Delta\Delta\phi} \\ \varepsilon_{\Delta\Delta\kappa} \end{pmatrix}_{12}. \tag{13}$$

The ROP stability conditions can be incorporated either as absolute constraints (He et al., 1992) or weighted constraints. If the constraints are weighted, the option used here, they can be easily added to the least-squares normal equations by the summation-of-normals method. In the implementation in this work, each constraint can be individually weighted by specifying a standard deviation. In practice, however, they are weighted as groups. A single standard deviation is defined for the group of base vector stability constraints. Likewise, a standard deviation is defined for the group of relative-angle stability constraints.

The weighted constraints approach has the advantage of flexibility. The constraints can be effectively turned on or off. That is, they can be added if doing so is deemed to be appropriate: when the ROPs are indeed stable. Specifying very low group standard deviations allows the constraints to effectively become absolute constraints. In a complementary way, the ROP stability can be assessed using the residuals of the weighted constraints. Sensor stability is an important issue and many efforts have been devoted to the subject (for example, Shortis et al., 2000; Habib et al., 2014). Furthermore, if there is a large sample of added constraints then they, along with other observable quantities, can be appropriately weighted by analysing the estimated variance components.

Self-calibrating Bundle Adjustment

The self-calibrating bundle adjustment problem is formulated in terms of a constrained Gauss–Markov model. The general form of the linearised image coordinate observations is partitioned into three parameter groups:

$$\mathbf{A}_e\widehat{\boldsymbol{\delta}}_e + \mathbf{A}_i\widehat{\boldsymbol{\delta}}_i + \mathbf{A}_o\widehat{\boldsymbol{\delta}}_o + \boldsymbol{w_p} = \widehat{\boldsymbol{v}}_{\boldsymbol{p}} \tag{14}$$

where $\mathbf{A}_e$, $\mathbf{A}_i$ and $\mathbf{A}_o$ are the design matrices for the EOPs, the IOPs and the object point coordinates, respectively; $\widehat{\boldsymbol{\delta}}_e$, $\widehat{\boldsymbol{\delta}}_i$ and $\widehat{\boldsymbol{\delta}}_o$ represent the correction vectors to the initial values for these three groups of parameters; $\mathbf{w}_p$ is the misclosure vector; and $\mathbf{v}_p$ is the vector of residuals. The associated weight matrix for this group of observations is denoted as $\mathbf{P}_\mathrm{p}$. The linearised ROP stability constraints are given by:

$$\boldsymbol{A}_e\widehat{\boldsymbol{\delta}}_e + \boldsymbol{w_p} = \widehat{\boldsymbol{v}}_{\boldsymbol{p}} \tag{15}$$

where $\mathbf{A}_c$, $\mathbf{w}_c$ and $\mathbf{v}_c$ are the design matrix, misclosure vector and residual vector, respectively. The weight matrix for the constraints is denoted as $\mathbf{P}_\mathrm{c}$. The network datum is defined by inner constraints imposed on the object points:

$$\mathbf{G}_o^T\hat{\boldsymbol{\delta}}_o = \mathbf{0} \tag{16}$$

where $\mathbf{G}_o$ is the design matrix. All EOPs, IOPs and object points are simultaneously estimated in a multistation, self-calibrating bundle adjustment of equations (13)–(16) using established procedures (Luhmann et al., 2014).

Experiments

Calibration Facility

Three datasets were captured with the Ladybug5 system in a dedicated indoor calibration laboratory at the University of Calgary: two for calibration and one for accuracy assessment. The laboratory is a temperature- and lighting-controlled environment and has nominal dimensions of 11 m × 11 m × 4 m. Some 500 Bubble-X targets are mounted on the floor, the ceiling and the walls of the lab (Fig. 2). Bubble-X is an extruded plastic with two outer skin layers and an internal lattice structure that makes it considerably stiffer than paper or cardboard printed targets. It is a lightweight material and is not influenced by humidity. The target pattern comprises a white circle on a black background that is printed directly on the matte-finish surface. Several different target sizes exist in the room. Those with 125 mm radius were used for this work. Some temporary paper targets were also mounted on the floor to densify the network.

Networks

For calibration dataset 1, images were captured from three nominal locations with the Ladybug5 upright (Fig. 3(a)). At each location, nine sets of images were captured. The camera system was rotated about its vertical axis by approximately 40° between acquisitions so that the entire room was imaged by each of the horizontal cameras. This also provided convergent imaging geometry for the horizontal cameras and roll diversity for the vertical camera. Scale variation for the vertical camera imagery was provided by depth variation in the target field itself: targets positioned at different heights on the unfinished ceiling and on the walls were observed. Unfortunately, however, this network design did not include roll angle diversity for the horizontal cameras. Note that many targets on the east side of the room (right in Fig. 3(a)) were omitted due to very narrow intersection angle geometry. Both these issues were rectified in calibration dataset 2.

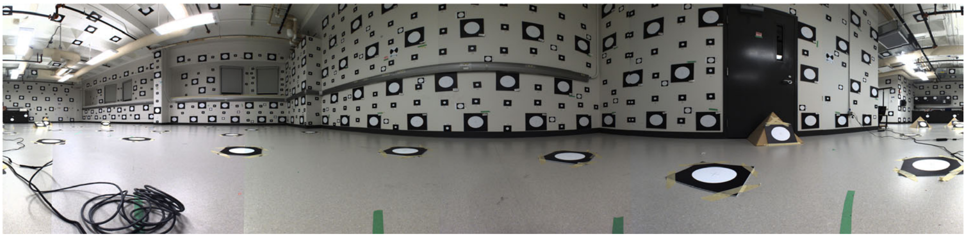

FIG. 2. Indoor calibration laboratory.

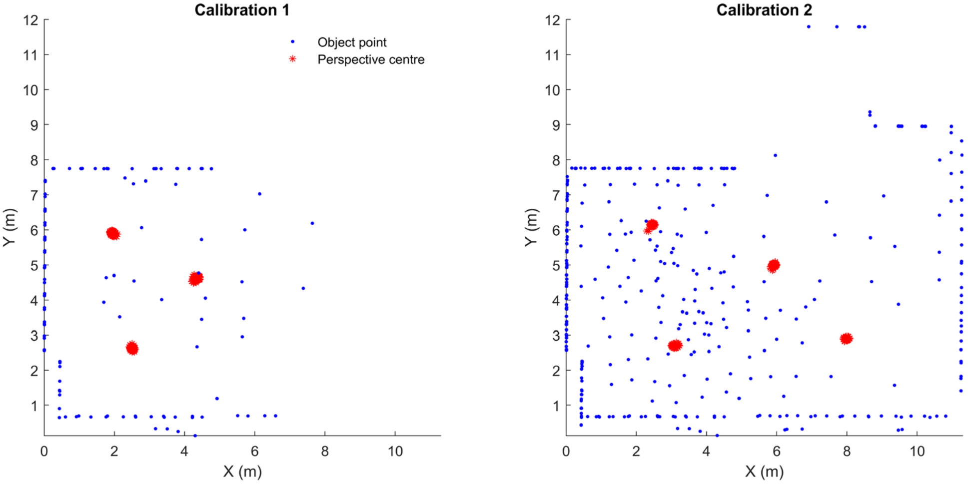

(a) (b)

FIG. 3. Calibration networks. (a) Calibration dataset 1. (b) Calibration dataset 2 (10 months after (a)).

Following a 10-month period during which the Ladybug5 was deployed on a vehicle-borne MMS and used for many data collection missions, calibration dataset 2 was captured with an improved network design (Fig. 3(b)). This also provided an opportunity to quantify any changes in camera system geometry due to usage. The calibration network was densified with additional temporary, paper targets affixed to the floor in order to provide a more uniform distribution of observed points in the image plane. The network comprised four nominal camera locations. Three were approximately at the same positions as in calibration 1 while the fourth was closer to the east wall (right in Fig. 3(b)) so those targets could be imaged with improved intersection geometry. Some highly tilted images were also incorporated in the network. The Ladybug5 system was mounted on a monopod and inclined up to 45° in two orthogonal directions at each nominal location. This provided the necessary roll diversity for the horizontal cameras. An Xsens MTI series inertial measurement unit was temporarily affixed to the camera system to observe the approximate EOP values needed for the target measurement algorithm and subsequent bundle adjustment.

Accuracy Assessment

The targets were independently surveyed to provide reference 3D coordinates for accuracy assessment. A single, high-resolution scan was acquired from the centre of the room with a Faro Focus 3D terrestrial laser scanner (TLS). A circular patch around each target was manually extracted from the point cloud. The centre coordinates were estimated using the method described by Lichti et al. (2019b). Past experience with this instrument has demonstrated that millimetre-level 3D coordinate accuracy can be achieved in a similar environment with comparable dimensions (Lichti et al., 2019a).

Following the acquisition of calibration dataset 1, additional images were captured in the indoor calibration laboratory. These were used for accuracy assessment to quantify the effectiveness of the modelling approach proposed herein. The imagery was acquired from two exposure stations separated by 2·8 m. These images were not used for the calibration but for independent accuracy assessment.

A total of 96 check points were observed in 10 horizontal images. Each image contained between 8 and 40 check points; all but two contained 20 or more. Almost all check points were observed in either two or three images. Two check points were observed in four images. The check points were estimated as tie points in the bundle adjustment. The ray intersection geometry of the tie points varied considerably, including both weakly and strongly determined points. Four control points in the corners of the network were fixed in the ensuing bundle adjustment to ensure that the estimated and reference coordinates from the TLS were in the same system. Check point coordinate differences were computed by subtracting the reference TLS coordinates from the photogrammetrically estimated values and the root mean square error RMSE_{XYZ} (Remondino et al., 2017) computed. Several different adjustment cases were performed for the accuracy assessment. These are described in more detail in subsequent sections.

Image Point Measurement

Images were captured in JPEG format since this is the standard operating procedure when the Ladybug5 is deployed as part of a vehicular MMS. The RGB colour imagery was converted to greyscale imagery (*Grey*) according to the International Commission on Illumination CIE 1931 colour space model:

$$Grey = 0.2125R + 0.7154G + 0.0721B \tag{17}$$

where R, G and B are the red, green and blue components, respectively.

Measurement of the 2D target centre coordinates was performed using the automated detection and labelling algorithm described in Jarron et al. (2019b). The major steps of the algorithm can be summarised as follows. Adaptive local thresholding of the greyscale image was performed followed by connected components analysis to label each region in the resulting binary image. Ellipse fitting based on the random sample consensus (RANSAC) was performed to eliminate outliers, which was followed by a final least-squares ellipse fit. A number of diagnostic tests were made to eliminate non-target regions. Prior knowledge, such as approximate camera height, was utilised for some of the EOPs while a range of candidate values was assumed for other EOPs. The known 3D target coordinates of the calibration room were projected into the image using the EOPs and nominal camera IOPs. The image point corresponding to each projected object point was selected according to the minimum distance. This process was accompanied by tests to reduce the occurrence of incorrect labelling.

Relative Orientation Stability Constraint Weighting

As mentioned, the weighted-constraints approach offers great flexibility for the enforcement of ROP stability. Here, three enforcement schemes were investigated: no constraints; small variances; variances set by approximate iterative variance component estimation (VCE). The high weights of the second approach meant that the constraints were effectively absolute. The aim of the third approach was to determine the weights of each group of observables (image coordinates, base vector stability constraints and relative-angle stability constraints) such that their relative contribution is approximately equivalent.

Experiment Results

Adjustment Metadata

Table I provides a high-level summary of the two calibration datasets. Overall, calibration 2 comprised fewer images (and, hence, fewer ROP stability constraints) but had more object points, image point observations and degrees of freedom. As can be seen in Fig. 4, the observations of datasets 1 and 2 cover nearly the entire image plane, respectively, reaching 94% and 91% of the maximum radial distance of 1596 pixels. The distribution of observations was improved in the second dataset thanks to the additional targets on the floor.

Interior Orientation Parameter Estimates

The estimates and the precision of the basic IOPs from the two calibration datasets are tabulated in Table II. Note that these results are from the case of very small variances for the ROP stability constraints. The horizontal cameras' x_p precision is about 25% lower than that of y_p for calibration 1 due to the aforementioned lack of roll diversity. The inclusion of highly tilted imagery in the second calibration dataset yielded the desired homogeneous precision. The principal point precision for the vertical camera was homogeneous for both calibrations due to the network design.

Principal distance precision among the horizontal cameras was homogeneous in both datasets, with the first being slightly higher. In both cases, the vertical camera's precision is lower. In the first case, this is due to the lack of convergent imaging while in the second case it was due to the lower number of observations appearing in the vertical camera imagery. The scale variation did successfully de-correlate the principal distance from the EOPs in the first calibration, as the largest correlation coefficient with the perspective centre

Table I. Calibration dataset metadata.

	Calibration 1	*Calibration 2*
No. of images	262	206
No. of object points	119	362
No. of observed image points	6314	9742
No. of ROP stability constraint sets	627	402
Total degrees of freedom	11 903	17 913
Maximum observed radial distance (pixels)	1495	1456

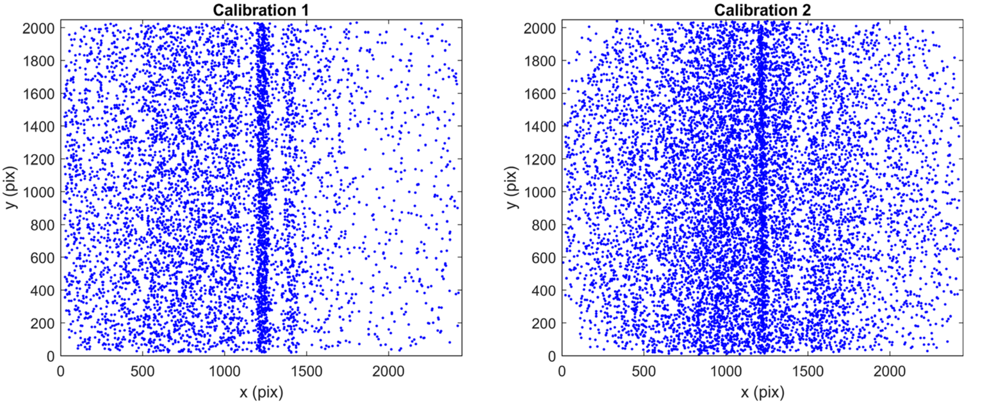

FIG. 4. Image point distribution for the calibration datasets (all images, all cameras).

TABLE II. Estimated interior orientation parameters (x_p, y_p, c) and their standard deviations σ from the two calibration datasets.

IOP	*Calibration*	*Horizontal cameras*					*Vertical*
		0	*1*	*2*	*3*	*4*	*5*
x_p	1	**1208·61**	1205·25	1235·22	1226·66	1234·21	**1218·00**
	2	**1209·08**	1205·49	1234·85	1226·73	1234·33	**1218·36**
σ	1	0·16	0·16	0·15	0·15	0·15	0·07
	2	0·11	0·12	0·12	0·11	0·11	0·14
y_p	1	**1012·74**	**1020·37**	1016·62	1000·33	1021·52	**1016·47**
	2	**1011·95**	**1019·99**	1016·57	1000·16	1021·81	**1017·85**
σ	1	0·12	0·11	0·11	0·11	0·12	0·06
	2	0·12	0·13	0·13	0·12	0·12	0·13
c	1	1234·91	1235·86	**1239·54**	1240·38	1239·51	**1239·46**
	2	1235·25	1235·82	**1238·95**	1240·11	1239·08	**1237·34**
σ	1	0·18	0·17	0·17	0·18	0·19	0·35
	2	0·22	0·22	0·21	0·21	0·22	0·59

Pairs of parameter estimates that are significantly different are shown in **bold**. All figures in pixels.

position was 0·2. In the second calibration, the introduction of highly convergent vertical camera images meant that many targets on the unfinished ceiling were partially or completely occluded by ductwork, electrical conduit, water pipes and light fixtures. As a result, the precision is lower. However, de-correlation from the EOPs was also achieved as the largest correlation was 0·15.

Analysing Table II reveals there are differences in the basic IOPs of the two calibration datasets. All are 0·8 pixels or less except for y_p and the principal distance of the vertical camera, which are about 1·4 and 2·1 pixels, respectively. These can be explained by the network differences already described. Under the reasonable assumption that the parameter estimates from the two datasets are uncorrelated, statistical testing was performed to assess the significance of these differences. Seven parameters were identified as significantly different at the 95% confidence level. Noting, however, that the linear equivalent of 0·8 pixels in image space is approximately 6 mm in object space, which is smaller than the mean object point precision from the check point analysis (see next section), these results

TABLE III. Model fit as a function of increasing the number of radial lens distortion terms for calibration 1.

Radial lens distortion model terms	*RMS_{xy} (pix)*	*% improvement*
k_1, k_2	4·94	–
k_1, k_2, k_3	1·21	73
k_1, k_2, k_3, k_4	0·45	90
k_1, k_2, k_3, k_4, k_5	0·38	92

suggest that the remaining parameters of the interior geometry were stable over the time between calibrations.

Radial Lens Distortion

The development of the radial lens distortion model is demonstrated with calibration dataset 1 without enforcement of the relative orientation constraints. If the constraints are heavily weighted, their addition to the bundle adjustment can lead to inflation of the image point RMS. Thus, they were omitted so as to prevent possible biases in this model development exercise.

The model fit following sequential addition of lens distortion terms is reported in Table III. The RMS_{xy} values are pooled estimates from all six cameras. The "base" model comprises the first two terms, k_1 and k_2. The adjustment including only k_1 did not converge due to the extreme barrel distortion of the Ladybug5 system. The RMS_{xy} estimates show a clear, but gradually diminishing, improvement as a result of including each successive radial lens distortion term. The final, five-term model exhibits an improvement amounting to an order of magnitude over the initial two-term model. Analysis of the AIC revealed that the final model was indeed superior to the others. Note that the final RMS_{xy} is lower than that reported in Table I due to omission of the ROP stability constraints.

Graphical analyses were used to support the model development. The scatter plots in Fig. 5 represent the superimposition of the radial component for all residuals (v_r) from all

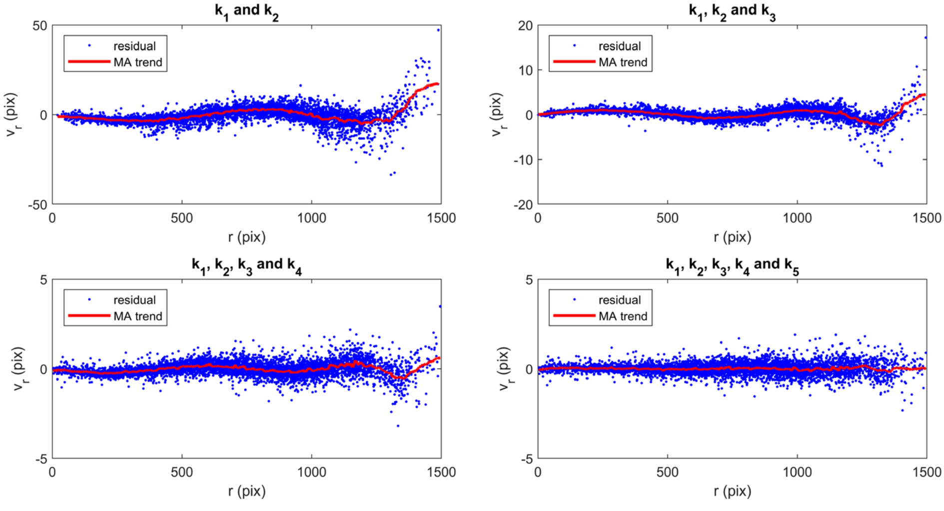

FIG. 5. Radial component of the image point residuals (v_r) in blue and moving average (MA) trend in red for calibration 1. Radial distances from 0 to 1495 pixels.

TABLE IV. Radial lens distortion term significance for calibration 1.

Radial lens distortion model terms	*Total number of terms*	*Number of significant terms*
k_1, k_2	12	12
k_1, k_2, k_3	18	18
k_1, k_2, k_3, k_4	24	24
k_1, k_2, k_3, k_4, k_5	30	29

TABLE V. Sample correlation coefficient matrix for radial lens distortion coefficients.

	k_1	k_2	k_3	k_4	k_5
k_1	1				
k_2	−0·974	1			
k_3	0·931	−0·988	1		
k_4	−0·885	0·962	−0·993	1	
k_5	0·843	0·933	0·976	−0·995	1

TABLE VI. Accuracy assessment as a function of the number of radial lens distortion terms for calibration 1.

Radial lens distortion model terms	*Mean difference (mm)*	*$RMSE_{XYZ}$ (mm)*	*% improvement*
k_1, k_2	8	152	–
k_1, k_2, k_3	10	36	76
k_1, k_2, k_3, k_4	3	18	88
k_1, k_2, k_3, k_4, k_5	2	10	93

six cameras. The moving average (MA) trends show the presence of unmodelled systematic distortions, except in the final model using all five terms. Note that unmodelled trends do not reflect the exact behaviour of the missing term(s) but rather the residual errors from the other terms trying to compensate for the missing terms, hence the multiple concavities in the first three models in Fig. 5. The final case, with all five terms k_1 to k_5, shows a flat MA trend, indicating that all systematic effects have been modelled up to the maximum observed radial distance of 1495 pixels.

The statistical significance of each radial lens distortion term was evaluated. In all four model cases, all terms are significant at the 95% confidence level with only one exception: k_2 for the vertical-looking camera with the full five-term model (Table IV). In this instance, the test value was 1·92, so it was in fact only marginally insignificant. Statistical testing for the second calibration dataset revealed that all 30 terms of the full model were significant. These outcomes, should, however, be tempered by the fact that high correlations – that are ignored in the individual significance testing – exist among the radial lens distortion coefficients. An example of the correlation coefficients for one camera is given in Table V. Some are quite large. Importantly, though, there were no high correlations with any of the EOPs; the largest coefficient was 0·46.

The best measure of the effectiveness of the radial lens distortion model is the independent accuracy assessment with check points (Table VI). Similarly to the results in Table III, the addition of each model term results in a significant, but diminishing, improvement. A bias of up to 1 cm exists in the first two models and the third case does not meet precision expectations. The five-term model is the only one for which the $RMSE_{XYZ}$ met the expected accuracy of 13 mm, the mean tie point coordinate precision. Thus, despite

Table VII. Derived relative orientation parameter statistics. Note the different units for the RMS_{angle} column.

Calibration	*ROP stability enforcement*	*RMS_{xy} (pixel)*	*RMS_{base} (mm)*	*RMS_{angle} (°/″)*
1	None	0·38	2·48	2·16°
1	Small variance	0·48	0·002	0·04″
1	VCE	0·42	0·28	26″
2	None	0·61	1·93	3·76°
2	Small variance	0·66	0·000	0·04″
2	VCE	0·62	0·24	23″

the high correlations between terms, the inclusion of five radial lens distortion terms improves the solution within a laboratory setting.

Both decentring distortion parameters were statistically significant for both calibration datasets. However, the decentring effect is considerably smaller than that of the radial lens distortion. The decentring profile reaches only 2·1 pixels at the maximum radial distance. Therefore, decentring distortion was not analysed further.

Model Fit and Relative Orientation Parameters

Table VII reports the RMS for the image points, the base vector components and the relative angles. The ROPs were derived from the estimated EOPs following adjustments with all three enforcement schemes. Regardless of the weighting scheme used, the quality of the fit of the observations to the sensor model is slightly lower in the second dataset. For both datasets, the imposition of the small-variance ROP stability constraints had the effect of inflating the RMS_{xy}. However, the constraints were clearly effective in enforcing ROP stability as the RMS values varied from a couple of millimetres and a couple of degrees to insignificant figures. The constraint enforcement case with VCE-derived weights had less impact in terms of inflating the image point coordinate residuals. ROP stability was enforced to the level of about one-quarter of a millimetre for base vector components and less than one-half of an arc minute for the relative angles.

Differences between the ROPs of the two calibrations were computed for the small-variance enforcement scheme. The statistics are presented in Table VIII. The results suggest that even after repeated use, the relative geometry of the Ladybug5 system is stable at the 1 to 2 millimetre level.

Accuracy Assessment – ROP Stability Constraints

As mentioned, several adjustments were performed for the accuracy assessment. Predetermined IOPs were implemented as constants and predetermined ROPs, implemented as weighted constraints (equations (7), (10), (11) and (12)) with small variances so as to effectively make them absolute constraints. IOP and ROP estimates from all three weighting

Table VIII. Statistics of the differences between the derived relative orientation parameters from calibrations 1 and 2.

	Base vector components (mm)	*Relative angles (″)*	*Linear equivalent at 10 m (mm)*
Mean	−0·5	−25	−1·2
Maximum	1·9	79	3·8
RMS	0·8	40	1·9

TABLE IX. Accuracy assessment statistics. All weighting schemes are "small variance" unless otherwise indicated.

	$RMSE_{XYZ}$ (mm)	% improvement	3D coordinate difference range (mm)	% improvement
Factory ROPs, x_p, y_p and c, our lens distortions (calibration 1)	133	–	1391	–
Factory ROPs, our IOPs (calibration 1)	76	43	675	52
Our IOPS, no ROPs (calibration 1)	10	92	95	93
Our IOPs and ROPs (calibration 1)	9	93	68	95
Our IOPs and ROPs (calibration 2)	10	92	95	93
Our IOPs and ROPs (calibration 1, VCE)	7	95	49	96
Our IOPs and ROPs (calibration 2, VCE)	10	92	94	93

schemes were tested. Each adjustment comprised 198 degrees of freedom. Jarron et al. (2019a) provide an initial report on differences between estimated and factory calibration parameters. Since very large differences between radial lens distortion profiles beyond $r = 1000$ pixels are reported, the factory-determined values were not used. Several combinations of factory parameters and parameters determined by this paper's methodology were tested and are summarised in Table IX.

The first case, using factory ROPs, some factory IOPs and the authors' lens distortion coefficients, shows decimetre-level agreement of photogrammetrically determined and scanned coordinates, but the range in coordinate differences is greater than metre-level. The large differences exist at weakly determined points that nominally lie on the baseline between camera stations (Fig. 6). Utilising all author-derived IOPs considerably improves the results by 43% in $RMSE_{XYZ}$ and 52% in terms of the 3D coordinate difference range. The 3D range is the diagonal of the rectangular prism spanned by the range of coordinate differences in each dimension. Centimetre-level accuracy is achieved with IOPs (without known ROPs enforced). Adding the known ROPs as constraints does not improve accuracy in terms of $RMSE_{XYZ}$ but does reduce the range of coordinate differences. The improvement is gained in the outliers that occur at the narrow intersection angles (Fig. 6). Without the ROP constraints, the differences in any one coordinate were up to 4 cm. With the

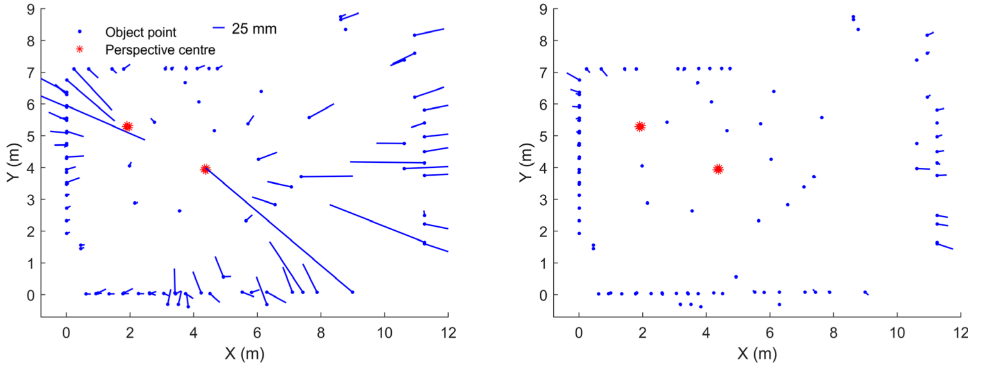

FIG. 6. Check point coordinate differences. Left: with factory ROPs, x_p, y_p and c, the authors' lens distortions (calibration 1). Right: with the authors' IOPs and ROPs (calibration 1).

TABLE X. Number of correlation coefficients with a magnitude greater than 0·9.

Calibration	*ROP stability enforcement*	*EOP–EOP*	*EOP–IOP*
1	None	226	0
1	Small variance	20 168	754
1	VCE	218	36
2	None	184	26
2	Small variance	8957	512
2	VCE	182	52

constraints, differences were up to 3 cm. Using the IOPs and ROPs from the second calibration produced similar results, though the range of differences was degraded slightly due to the changes in parameters reported in Tables II and VIII.

For all cases discussed in the preceding paragraph, the IOPs and ROPs were derived from the small-variance weighting scheme. Use of the parameters from the VCE weighting scheme (final two rows of Table IX) produced comparable accuracy to that achieved with the small-variance parameters. In fact, the calibration 1 results are slightly superior in terms of both measures. The slightly less accurate results using the calibration 2 parameters are in line with the findings above.

ROP Stability Constraints – Parameter Correlations

The ROP stability constraints impose functional dependencies between EOPs. Although their effectiveness has been demonstrated, the question of whether the solution is degraded by the small-variance weighting remains. Therefore, an analysis of correlations among EOPs and with IOPs has been undertaken. Table X presents a summary of large correlation coefficients, defined as having a magnitude greater than 0·9, for all three weighting schemes for both datasets.

Using the unconstrained case as a benchmark, imposing the small-variance stability constraints increases the number of high EOP–EOP correlations by nearly two orders of magnitude for both calibrations. The high correlations in the unconstrained case are due to local weaknesses in network geometry that were exacerbated by the constraints. Interestingly, the VCE weighting actually reduces, albeit very slightly, the number of high EOP–EOP correlations, so there is no adverse effect caused by their introduction.

The low number of high EOP–IOP correlations in the unconstrained case demonstrates the success of the network design to reduce projective compensation. The use of the small-variance constraints introduces several hundred high correlations. The VCE weighting does introduce some correlations, but the number is an order of magnitude smaller.

It should be borne in mind that the total number of off-diagonal elements in the parameter correlation matrices is large: 3 942 210 and 5 671 542 for calibrations 1 and 2, respectively. Thus, the percentage of large correlations in the small-variance case is less than 1%. However, the introduction of these dependencies may be the cause of the slightly worse results for the small-variance accuracy assessment for calibration 1 in comparison with the VCE results. In terms of good practice, the VCE enforcement approach is recommended since it avoids the introduction of adverse correlations.

CONCLUSIONS

An approach for the geometric modelling and calibration of a multi-camera, spherical imaging system, the Ladybug5, has been presented. Results from multiple calibration datasets were presented to demonstrate the effectiveness of the methodology. Image coordinate observations agreed with the model at the sub-pixel level. Centimetre-level 3D reconstruction accuracy in object space was achieved using the parameters determined with the proposed approach. Accuracy was improved by 95% over what could be achieved using the manufacturer's IOPs and ROPs. The severe barrel distortion caused by the system's wide-angle lenses necessitated the adoption of a five-term radial lens distortion model. Although this is unconventional and the distortion coefficients are inherently very highly correlated, it was found to be successful. Inclusion of five radial lens distortion terms led to a 92% improvement in model fit in terms of residual RMS and a 93% improvement in 3D object space accuracy. The relative position and orientation of the system's six cameras were effectively modelled with relative orientation stability constraints implemented as weighed constraints. Analysis of the system calibration after a 10-month period of usage revealed sub-pixel stability of most IOPs and millimetre-level stability of the ROPs.

Two different approaches to weighting the ROP stability constraints were investigated. It may be tempting to enforce the constraints rigidly with very small variances (high weights) to accurately model the assumed mechanical stability among the individual sensors of a multi-camera system. However, the approach of determining the stability constraint weights using VCE has been demonstrated to be superior for the calibration of the Ladybug5 system. The relaxed weighting achieved comparable (or slightly better) accuracy, did not introduce adverse parameter correlations and resulted in only minor inflation of the image point coordinate residuals.

A number of possibilities for future work exist. Perhaps paramount among these is the possibility to model wide-angle lenses like those of the Ladybug5 with a fisheye lens model. A preliminary investigation of this approach yielded promising results (Jarron et al., 2019c). The concept is the fisheye model compensates for the majority of the barrel distortion, leaving only a residual radial lens distortion signal that should require fewer coefficients. Although the high correlations between coefficients did not degrade the results in this study, it would be advantageous to utilise a model free from strong functional dependencies as a general principle. Scope exists for future investigation into the use of the VCE weighting for the ROP stability constraints applied to other multi-camera systems and the exact correlation mechanisms. Future work may also include a stability test of calibration with temperature changes or physical impact when used for mapping.

Acknowledgements

Funding for this research was provided by the Natural Sciences and Engineering Research Council of Canada and McElhanney Ltd.

References

Agisoft LLC, 2018. *Agisoft PhotoScan User Manual Professional Edition*, Version 1.4. 121.

Akaike, H., 1974. A new look at the statistical model identification. *IEEE Transactions on Automatic Control*, 19(6): 716–723.

Bosch, J., Gracias, N., Ridao, P. and Ribas, D., 2015. Omnidirectional underwater camera design and calibration. *Sensors*, 15(3): 6033–6065.

Brown, D. C., 1966. Decentering distortion of lenses. *Photogrammetric Engineering*, 32(3): 444–462.

Brown, D. C., 1971. Close-range camera calibration. *Photogrammetric Engineering*, 37(8): 855–866.

Campos, M. B., Tommaselli, A. M. G., Marcato Junior, J. and Honkavaara, E., 2018. Geometric model and assessment of a dual-fisheye imaging system. *Photogrammetric Record*, 33(162): 243–263.

Cui, T., Ji, S., Shan, J., Gong, J. and Liu, K., 2017. Line-based registration of panoramic images and LiDAR point clouds for mobile mapping. *Sensors*, 17(1): 70.
Detchev, I., Habib, A., Mazaheri, M. and Lichti, D., 2018. Practical in-situ implementation of a multicamera multisystem calibration. *Journal of Sensors*, 2018: 1–12.
Habib, A., Kersting, A. P., Bang, K.-I. and Rau, J., 2011. A novel single-step procedure for the calibration of the mounting parameters of a multi-camera terrestrial mobile mapping system. *Archives of Photogrammetry, Cartography and Remote Sensing*, 22: 173–185.
Habib, A., Detchev, I. and Kwak, E., 2014. Stability analysis for a multi-camera photogrammetric system. *Sensors*, 14(8): 15084–15112.
He, G., Novak, K. and Feng, W., 1992. On the integrated calibration of a digital stereo-vision system. *International Archives of Photogrammetry and Remote Sensing*, 29(B5): 139–145.
Jarron, D., Lichti, D., Shahbazi, M. and Radovanovic, R., 2019a. Multi-camera panoramic imaging system calibration. *11th International Conference on Mobile Mapping Technology*, Shenzhen, China. Pages 70–77.
Jarron, D., Shahbazi, M., Lichti, D. and Radovanovic, R., 2019b. Automatic detection and labelling of photogrammetric control points in a calibration test field. *International Archives of the Photogrammetry, Remote Sensing and Spatial Information Sciences*, 42(2/W13): 1673–1680.
Jarron, D., Shahbazi, M., Lichti, D. and Radovanovic, R., 2019c. Modelling wide-angle lens cameras for metrology and mapping applications. *ISPRS Annals of Photogrammetry, Remote Sensing and Spatial Information Sciences*, 4(2/W7): 79–86.
Khoramshahi, E. and Honkavaara, E., 2018. Modelling and automated calibration of a general multi-projective camera. *Photogrammetric Record*, 33(161): 86–112.
King, B. A., 1995. Bundle adjustment of constrained stereopairs-mathematical models. *Geomatics Research Australasia*, 63: 67–92.
Lerma, J. L., Navarro, S., Cabrelles, M. and Seguí, A. E., 2010. Camera calibration with baseline distance constraints. *Photogrammetric Record*, 25(130): 140–158.
Lichti, D. D., Sharma, G. B., Kuntze, G., Mund, B., Beveridge, J. E. and Ronsky, J. L., 2015. Rigorous geometric self-calibrating bundle adjustment for a dual fluoroscopic imaging system. *IEEE Transactions on Medical Imaging*, 34(2): 589–598.
Lichti, D. D., Glennie, C. L., Jahraus, A. and Hartzell, P., 2019a. New approach for low-cost TLS target measurement. *ASCE Journal of Surveying Engineering*, 145(3): article 04019008. 12 pages.
Lichti, D. D., Glennie, C. L., Al-Durgham, K., Jahraus, A. and Steward, J., 2019b. Explanation for the seam line discontinuity in terrestrial laser scanner point clouds. *ISPRS Journal of Photogrammetry and Remote Sensing*, 154: 59–69.
Lichti, D. D., Jarron, D., Shahbazi, M., Helmholz, P. and Radovanovic, R., 2019c. Investigation into the behaviour and modelling of chromatic aberrations in non-metric digital cameras. *ISPRS – International Archives of the Photogrammetry, Remote Sensing and Spatial Information Sciences*, 42(2/W18): 99–106.
Luhmann, T., Robson, S., Kyle, S. and Boehm, J., 2014. *Close-range Photogrammetry and 3D Imaging*. Second edition. De Gruyter, Berlin, Germany. 702 pages.
Photometrix, 2016. *CameraCalibrator User Manual*, Version 2.0. 47 pages.
Rau, J. Y., Su, B. W., Hsiao, K. W. and Jhan, J. P., 2016. Systematic calibration for a backpacked spherical photogrammetry imaging system. *International Archives of Photogrammetry, Remote Sensing and Spatial Information Sciences*, 41(B1): 695–702.
Remondino, F., Nocerino, E., Toschi, I. and Menna, F., 2017. A critical review of automated photogrammetric processing of large datasets. *International Archives of Photogrammetry, Remote Sensing and Spatial Information Sciences*, 42(2/W5): 591–599.
Schneider, J. and Förstner, W., 2013. Bundle adjustment and system calibration with points at infinity for omnidirectional camera systems. *Zeitschrift für Photogrammetrie, Fernerkundung und Geoinformation*, 4: 309–321.
Shortis, M., 2015. Calibration techniques for accurate measurements by underwater camera systems. *Sensors*, 15(12): 30810–30826.
Shortis, M. R., Ogleby, C. L., Robson, S., Karalis, E. M. and Beyer, H. A., 2000. Calibration modelling and stability testing for the Kodak DC200 series digital still camera. *Videometrics and Optical Methods for 3D Shape Measurement*, San Jose, California, USA. SPIE 4309: 148–153.
Tommaselli, A. M. G., Galo, M., de Moraes, M. V. A., Marcato Junior, J., Caldeira, C. R. T. and Lopes, R. F., 2013. Generating virtual images from oblique frames. *Remote Sensing*, 5(4): 1875–1893.
Wang, Y., Chen, Q., Zhu, Q., Liu, L., Li, C. and Zheng, D., 2019. A survey of mobile laser scanning applications and key techniques over urban areas. *Remote Sensing*, 11(13): article 1540. 20 pages.

Résumé

Le Ladybug5 est un système intégrant plusieurs caméras et caractérisé par un champ de vision quasi-sphérique. Il est couramment déployé en cartographie mobile en vue de l'acquisition d'images pour la reconstruction 3D. Cet article décrit une approche pour la modélisation géométrique et l'auto-calibration de ce système. Aux équations de colinéarité du modèle sténopé sont ajoutés cinq termes de distorsion optique pour corriger une forte distorsion en barillet. Des contraintes pondérées de stabilité de l'orientation interne sont prises en compte dans la compensation par faisceaux lors de l'auto-calibration afin de maintenir la stabilité angulaire et positionnelle entre les six caméras du système Ladybug5. Une précision centimétrique peut être atteinte dans la reconstruction 3D, avec un taux d'amélioration de 92% et 93% respectivement dans l'espace image et l'espace objet. L'expérience met en évidence sur une période de dix mois une stabilité sub-pixellaire pour l'orientation interne et une stabilité de niveau millimétrique pour l'orientation relative.

Zusammenfassung

Das integrierte Multikamerasystem Ladybug5 besitzt ein nahezu sphärisches Bildfeld. Es wird in vielen mobilen Mappingsystemen zur Bilddatenerfassung für eine 3D Modellierung eingesetzt. Dieser Beitrag stellt einen Ansatz für die Modellierung der Geometrie und die Selbstkalibrierung dieses Systems vor. Die Kollinearitätsgleichungen der Zentralprojektion werden um fünf Terme für eine radiale Verzeichnung ergänzt, um die starke tonnenförmige Verzeichnung zu korrigieren. Um die gegenseitige Lage- und Orientierungsstabilität der sechs Kameras des Ladybug5 Systems zu erzwingen werden gewichtete Stabilitätsbedingungen für die relative Orientierung zur Bündelausgleichung für die Selbstkalibrierung hinzugefügt. Damit können Genauigkeiten der 3D Rekonstruktion im Zentimeterbereich erzielt werden. Das bedeutet eine Steigerung der Präzision im Bildraum und Genauigkeit im Objektraum von 92% bzw. 93%, bezogen auf ein übliches Verzeichnungsmodell mit zwei Parametern. Über einen Zeitraum von zehn Monaten konnte die Stabilität der inneren Orientierung im Subpixel-Bereich und die Stabilität der relativen Orientierung im Millimeterbereich nachgewiesen werden.

Resumen

Ladybug5 es un sistema que integra múltiples cámaras captando un campo de visión casi esférico. Por lo general, se implementa en sistemas móviles de cartografiado recopilando imágenes para la captura de realidad 3D. Este artículo describe un modelo geométrico y de autocalibración para este sistema. Las ecuaciones de colinealidad del modelo de cámara estenopeica se han extendido con cinco términos de distorsión radial de la lente para corregir la severa distorsión de barril. Restricciones ponderadas de estabilidad de la orientación relativa se agregan a los parámetros de autocalibración en la solución de ajuste por haces para reforzar la estabilidad angular y posicional entre las seis cámaras del sistema Ladybug5. Se puede alcanzar una precisión en la reconstrucción 3D a nivel de centímetros. Comparándolo con un modelo de distorsión radial de solo dos términos se puede obtener una mejora de la precisión en el espacio imagen y en el espacio objeto de un 92% y 93% respectivamente. La orientación interior a nivel de subpíxeles y la orientación relativa a nivel milimétrico se han demostrado estables en un período de diez meses.

摘要

*Ladybug5*为一整合性多相机系统，具有近球形视野。常应用于行动制图系统，收集影像以搜集*3D*现况。本文提出对该系统几何建模和自率的一种方法。本方法采用共线式相机模型附加五个径向透镜畸变差参数，以校正严重的筒形透镜畸变。为提升*Ladybug5*的六个相机间角度与位置之稳定性，自率光束法平差中加入带权相对方位约制。本方法可以达成厘米级的*3D*重建，相对于两阶段的处理方式，本方法影像空间精度与物空间精度分别提高*92%*与*93%*。经由十个月的时间，实验还证实达成次像元内方位稳定度，以及相机间毫米级相对方位稳定性。